



AgentFoX: LLM Agent-Guided Fusion with eXplainability for AI-Generated Image Detection

Yangxin Yu¹ Yue Zhou¹ Bin Li^{1*} Kaiqing Lin¹ Haodong Li¹ Jiangqun Ni² Bo Cao^{3†}

¹Guangdong Provincial Key Laboratory of Intelligent Information Processing, Shenzhen Key Laboratory of Media Security, and SZU-AFS Joint Innovation Center for AI Technology, Shenzhen University, Shenzhen 518060, China

²School of Cyber Science and Technology, Sun Yat-sen University, China

³The Smart City Research Institute of China Electronics Technology Group Corporation, Shenzhen, China

2453043007@mails.szu.edu.cn, libin@szu.edu.cn

Abstract

*The increasing realism of AI-Generated Images (AIGI) has created an urgent need for forensic tools capable of reliably distinguishing synthetic content from authentic imagery. Existing detectors are typically tailored to specific forgery artifacts—such as frequency-domain patterns or semantic inconsistencies—leading to specialized performance and, at times, conflicting judgments. To address these limitations, we present **AgentFoX**, a Large Language Model-driven framework that redefines AIGI detection as a dynamic, multi-phase analytical process. Our approach employs a quick-integration fusion mechanism guided by a curated knowledge base comprising calibrated Expert Profiles and contextual Clustering Profiles. During inference, the agent begins with high-level semantic assessment, then transitions to fine-grained, context-aware synthesis of signal-level expert evidence, resolving contradictions through structured reasoning. Instead of returning a coarse binary output, AgentFoX produces a detailed, human-readable forensic report that substantiates its verdict, enhancing interpretability and trustworthiness for real-world deployment. Beyond providing a novel detection solution, this work introduces a scalable agentic paradigm that facilitates intelligent integration of future and evolving forensic tools.*

1. Introduction

The proliferation of AI-Generated Images (AIGI), marked by their remarkable realism, poses significant societal chal-

lenges such as sophisticated misinformation and hyper-realistic forgeries. The research community has responded with a diverse and rapidly growing array of specialized AIGI detectors, each engineered to capture distinct types of generative artifacts. For instance, some methods analyze the reconstruction residuals of diffusion models (e.g., DRCT [2]), others leverage frequency-domain analysis to identify latent upsampling fingerprints (e.g., SPAI [13]), while techniques like RINE [15] and Patch Shuffle [45] focus on visual concept inconsistencies and the isolation of non-semantic patterns, respectively. Because these models learn from fundamentally different forgery signatures, their performance is inherently context-dependent; a detector proficient in analyzing one class of images may be ineffective on another.

We empirically demonstrate the specialization of different methods in Fig. 1, which visualizes the consensus of correct detections among several signal-level expert detectors [2, 13, 15, 45]. The analysis reveals a stark contrast in consensus: while **55.83%** of samples are correctly identified by all experts, only **1.07%** are unanimously misclassified. The vast remainder of the dataset (**43.1%**) falls into a highly fragmented landscape of disagreement, where only specific subsets of detectors succeed. This fragmentation strongly indicates that **each detector possesses a unique “expertise”** and that a system capable of intelligently fusing their outputs could achieve superior robustness and generalization. However, traditional ensemble methods like meta-classifiers face critical deployment hurdles, as their reliance on expensive, data-intensive retraining creates rigid architectures unable to easily integrate new state-of-the-art (SoTA) detectors.

Currently, little prior work addresses the integration of multiple detectors, and rudimentary strategies such as

*Corresponding author.

†Code: <https://github.com/suncore946/AgentFoX>.
git

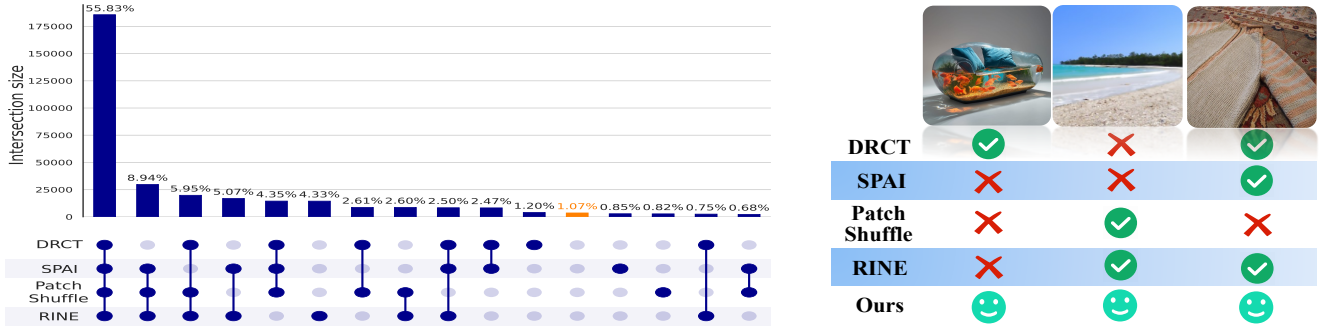


Figure 1. **Consensus and Disagreement Landscape Among AIGI Detectors.** Samples from seven publicly available datasets(Sect. 4.1). (Left) The UpSet plot quantitatively analyzes the performance of four expert detectors. (Right) Visual examples showcase these challenging cases of disagreement. Different experts fail on different images, creating conflicting signals.

majority voting fail to explain disagreements or adapt to image-specific semantics and context. To fill this gap, we propose **AgentFoX** — the first agent-driven multi-expert fusion framework for dynamic, multi-stage reasoning in AIGI detection. AgentFoX uses two pre-computed knowledge resources: **Expert Profiles** capturing detector reliability, and **Clustering Profiles** encoding contextual patterns in generated images. These priors enable zero-shot forensic reasoning without retraining and support rapid integration of new detectors. Guided by these profiles, the LLM agent fuses heterogeneous cues and resolves conflicts through rule-based reasoning. The rules follow guidelines derived from human forensic expertise, constraining decisions to avoid speculative outputs and ensuring that results remain transparent and evidence-backed.

In summary, the main contributions of this paper are as follows:

- We introduce **AgentFoX**, the first agent-guided multi-expert fusion framework for AIGI detection. Guided by pre-computed **Expert Profiles** (model-metrics) and **Clustering Profiles** (data-metrics), the agent fuses heterogeneous detectors, enabling zero-shot forensic reasoning without retraining and rapid adaptation to new detectors.
- We deliver **explainability in multi-expert AIGI detection** through a traceable reasoning paradigm. Our agent generates a transparent forensic report that justifies its verdict by documenting evidence, expert agreements, and the rationale for conflict resolution, replacing opaque aggregation with a fully auditable and interpretable workflow.
- We achieve superior accuracy and robustness on high-conflict AIGI and in-the-wild benchmarks, consistently outperforming individual detectors and conventional ensembles.

2. Related Work

Signal-level Expert Models in AIGI Detection Early AIGI detectors often relied on CNN architectures such as CNNSpot [35], trained on ProGAN and exhibiting notable cross-GAN generalization. Subsequent works, e.g., Uni-vFD [42] and RINE [15], improved generalization by fine-tuning CLIP-based visual encoders, demonstrating the benefits of leveraging foundation models. Later methods such as C2P-CLIP [34], RepDFD [20], and Effort [39] employed parameter-efficient fine-tuning (PEFT) to preserve pre-trained knowledge. Beyond encoder tuning, studies explored data augmentation and bias mitigation: OMAT [47] introduced adversarially generated semantic-bias samples, while DDA [3] and B-Free [8] utilized reconstructed image pairs. Auxiliary cues were also exploited; for instance, DIRE and DRCT investigated reconstruction discrepancies, while FatFormer [22] adopted frequency-domain representations. Despite these advances, many signal-level approaches remain dependent on specific low-level artifacts, inherently constraining their robustness against previously unseen forgery types.

MLLM-based AIGI Detection Recent advances in Multimodal Large Language Models (MLLMs) have led to their adoption in AI-generated image (AIGI) detection. Early attempts either fine-tuned MLLMs on instruction-following datasets [36, 44] or introduced rule-based reinforcement protocols [12, 37]. While both strategies help align models to the task, they remain constrained by the limited perceptual capacity of current MLLM vision encoders and often plateau at suboptimal accuracy [21].

To address these limitations, some works have paired MLLMs with external forensic experts, feeding their outputs or feature maps into the language model [4, 48]. This coupling can improve accuracy, but usually demands intricate alignment steps and resource-intensive VQA-style annotations, which limit scalability and rarely allow the com-

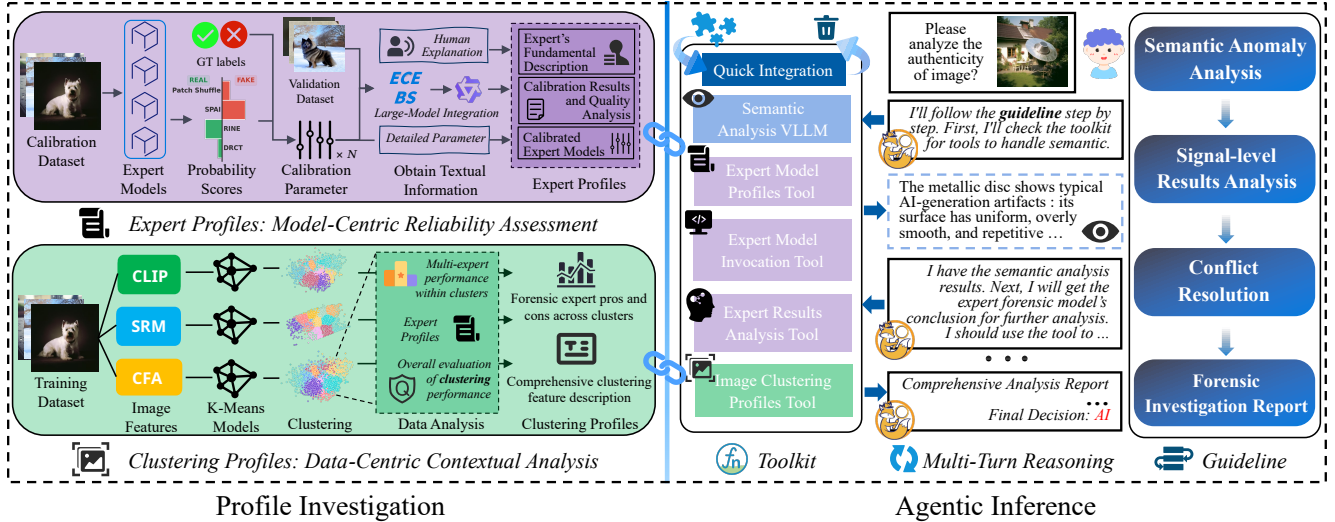


Figure 2. Overview of the **AgentFoX** framework. Left: **Profile Investigation** constructs *Expert Profiles* and *Clustering Profiles*. Right: **Agentic Inference** leverages these profiles through a Toolkit to conduct multi-stage forensic reasoning and compile an authenticity report.

bined system to surpass the best individual expert. AIGI-Holmes [48], for example, adopts a fixed fusion between a visual expert and an MLLM. The design is static and does not employ any agent-driven decision mechanism.

Agent-based approaches have emerged more recently, though their roles differ markedly. UniShield [11], for instance, deploys a perception agent that routes each image to one detection track—functioning as a task selector rather than a fusion engine—and does not reconcile conflicting predictions from multiple forensic sources. Similarly, Agent4FaceForgery [17] employs multi-agent interactions to synthesise diverse deepfake training data, but these agents operate entirely offline and are absent from real-time inference.

To our knowledge, no prior work equips an LLM-based agent to adaptively fuse multiple modality-specific AIGI detectors during inference—guided by expert profiling and with built-in interpretability. This capability is critical when heterogeneous experts capture complementary yet possibly conflicting forensic cues, requiring dynamic, content-aware resolution to ensure consistent and reliable decisions. Our framework addresses this gap by enabling an LLM-based agent to reason over the outputs of both a Vision–Language Large Language Model (VLLM) and specialised AIGI detectors, integrating them on a per-case basis. This context-dependent fusion substantially improves generalisation to unseen generators and outperforms any single model in isolation.

3. Method

Our proposed **AgentFoX** framework for AIGI detection consists of two decoupled components: **Profile Investigation**

(Sect. 3.1) and **Agentic Inference** (Sect. 3.2), as depicted in Fig. 2. This design enables the quick integration of new detectors via a one-time profiling step that can be performed without retraining the core agent or other existing experts. An LLM-based agent then leverages these calibrated, context-aware profiles to synthesise heterogeneous forensic evidence into a coherent, evidence-driven decision.

In **Profile Investigation**, we construct two complementary profiles: **Expert Profiles** to quantify each detector’s calibrated reliability, and **Clustering Profiles** to capture its context-dependent performance on semantic image clusters. During **Agentic Inference**, the agent follows a guideline-driven, ReAct-style [41] loop. It invokes tools to gather evidence from semantic and signal-level experts, audits their outputs, and resolves conflicts using context-aware reweighting informed by the profiles. This process culminates in a multifaceted and interpretable forensic report.

3.1. Profile Investigation

This offline phase builds a knowledge base to equip the agent with data-driven priors. We analyze each expert detector’s performance and the data’s statistical properties, distilling this information into two sets of LLM-interpretable profiles: *Expert Profiles* and *Clustering Profiles*. Details on data splits are in Sect. 4.1.

Expert Profiles: Model-Centric Reliability Assessment

Multiple heterogeneous signal-level experts produce confidence scores on whether an image is AI-generated, serving as the basis for agent-guided decisions. However, empirical calibration curves from large AIGI benchmarks [18] reveal systematic miscalibration—raw probability estimates are often overconfident relative to the true posterior. To en-

sure fair comparison across experts and provide the agentic framework with trustworthy decision metrics, we perform probability calibration, transforming raw scores into interpretable signals that are comparable across models.

Let $\mathcal{M} = \{M_1, \dots, M_N\}$ be a panel of N pre-trained AIGI detectors. For each expert M_j and image $I_i \in \mathcal{D}_{\text{train}}$, we obtain the raw prediction score $p_{ij} = M_j(I_i)$. These scores are calibrated using five widely adopted post-hoc, model-agnostic methods—Temperature Scaling [9], Platt Scaling [30], Isotonic Regression [25], Histogram Binning [43], and Beta Calibration [16]—with the mapping for method m and expert M_j denoted by $F_j^{(m)}$.

For each $F_j^{(m)}$, we compute the Expected Calibration Error (ECE) [26] on a disjoint validation set \mathcal{D}_{val} :

$$\text{ECE} = \sum_{b=1}^B \frac{|S_b|}{|\mathcal{D}_{\text{val}}|} |\text{acc}(S_b) - \text{conf}(S_b)|, \quad (1)$$

where S_b is the set of validation samples whose calibrated confidences fall into the b -th bin, and $\text{acc}(S_b)$ and $\text{conf}(S_b)$ are the bin-wise average accuracy and confidence, respectively. The optimal calibration function \hat{F}_j for M_j is then chosen as the one achieving the lowest ECE on \mathcal{D}_{val} .

For interpretability and smooth integration into agent-guided fusion, each expert is assigned a structured *Expert Profile* with clearly defined component properties, as:

$$\text{ExpertProfile}(M_j) = \{T_{\text{desc},j}^{\text{LLM}}, T_{\text{quality},j}^{\text{LLM}}, \hat{F}_j^{\text{TOOL}}\}, \quad (2)$$

where:

- $T_{\text{desc}}^{\text{LLM}}$ [**TEXT**]: a structured description of the expert’s core mechanism and typical strengths. This text, initially provided externally, is processed by an LLM into a standardized format that highlights contextual cues for the agent-guided fusion.
- $T_{\text{quality}}^{\text{LLM}}$ [**TEXT**]: an LLM-generated reliability report based on Expected Calibration Error (ECE) and Brier Score (BS) [7], summarizing calibration and probabilistic accuracy to assess the trustworthiness of the expert’s outputs and inform its weighting in AgentFoX’s fusion.
- \hat{F}_j^{TOOL} [**TOOL**]: an executable module that applies the selected calibration function \hat{F}_j to produce confidence-adjusted predictions for use in fusion orchestration.

Clustering Profiles: Data-Centric Contextual Analysis

Global metrics such as overall F1-score often conceal strong dependencies on image-specific context: a detector may perform well for certain textures or generation patterns but fail on others. Since these variations tend to form structured distributions in the feature space, clustering provides a natural way to capture such localized patterns and enable context-adaptive fusion. Therefore, we introduce a

data-centric contextual analysis module, termed Clustering Profiles, which informs AgentFoX to weight signal-level experts according to their local reliability—rather than relying solely on global performance metrics.

Given the training set $\mathcal{D}_{\text{train}}$, each image I_i is encoded as a heterogeneous feature vector \mathbf{x}_i that combines three complementary modalities t : CLIP [31] embeddings capturing semantic content, compact SRM [6] descriptors characterizing texture and noise statistics, and enhanced CFA [23] features representing spatial–frequency artifacts. Because the statistical characteristics of these modalities t differ, clustering is performed separately in each subspace:

$$\mathcal{C}_c^{(t)} = \text{KMeans}(\{\mathbf{x}_i^{(t)}\}_{i=1}^{|\mathcal{D}_{\text{train}}|}; K_t), \quad c \in \{1, \dots, K_t\}, \quad (3)$$

where $\mathbf{x}_i^{(t)}$ denotes the modality t feature vector of image I_i , $\mathcal{C}_c^{(t)}$ is the c -th cluster and K_t controls granularity.

At modality t , for each expert detector M_j and cluster c , we evaluate the local reliability on the validation split \mathcal{D}_{val} as $\Phi_{c,j}^{(t)} = (\text{F1}_{c,j}^{(t)}, \text{ACC}_{c,j}^{(t)})$, where F1 and ACC denote the F1-score and accuracy, respectively.

For each cluster c within modality t , we construct a **Cluster Reliability Profile**, denoted as $\mathcal{R}_c^{(t)}$. This profile is a **structured ranked list** of all expert detectors, ordered according to their local reliability scores $\Phi_{c,j}^{(t)}$. The *clustering quality profile* \mathcal{Q}_t is computed using the Silhouette coefficient [1] and the Davies–Bouldin index [5]; this score is then used by the agent to adaptively down-weight clusters exhibiting poor separability.

To formally encapsulate the modality-specific contextual characterization, we define the *Clustering Profile* for modality t as:

$$\text{ClusterProfile}(t) = \{T_{\mathcal{R}_c,t}^{\text{LLM}}, T_{\mathcal{Q},t}^{\text{LLM}}, \{\mathcal{C}_c^{(t)}\}^{\text{TOOL}}\}, \quad (4)$$

where:

- $T_{\mathcal{R}_c,t}^{\text{LLM}}$ [**TEXT**]: denotes an LLM-inferred synthesis that distills detector ranking patterns within each cluster c for modality t , providing semantic interpretations of localized model strengths and weaknesses.
- $T_{\mathcal{Q},t}^{\text{LLM}}$ [**TEXT**]: is an LLM-produced summary of clustering quality metrics \mathcal{Q}_t , capturing the trade-off between cluster compactness and separability.
- $\{\mathcal{C}_c^{(t)}\}^{\text{TOOL}}$ [**TOOL**]: an executable projection module that maps a new image to its modality- t cluster and retrieves the corresponding reliability profile \mathcal{R}_c for downstream fusion.

3.2. Agentic Inference

During the Agentic inference phase, for a given image I under investigation, our agent conducts a dynamic multi-phase forensic analysis, rather than the fixed pipelines adopted in

prior LLM-based detection methods [36, 37, 44]. This analysis is driven by a predefined forensic *guidelines*, denoted as \mathcal{G} , which is implemented as a structured, rule-based system prompt distilled from human forensic workflows. \mathcal{G} constrains LLM reasoning, mitigates instability and opacity, and ensures compliance with established investigative procedures for AI-generated image detection. The complete guidelines are provided in the Supplementary Material for reproducibility.

Operating within a multi-turn reasoning loop, **AgentFoX** leverages its **Toolkit** to query the **Profile Investigation** repository, retrieving *Expert Profiles* for model-centric reliability assessment and *Clustering Profiles* for data-centric contextual analysis. This two-fold integration forms a unified “reliability–context” view, enabling the agent to dynamically schedule experts based on their strengths and confidence assessments within the query’s contextual cluster. Through this profile-driven scheduling and subsequent evidence fusion, AgentFoX produces a final decision as a transparent synthesis of multi-source, context-aware evidence, rather than an opaque black-box output.

Stage 1: Semantic Anomaly Analysis

AgentFoX’s investigation begins with a holistic, semantic level assessment. It invokes a specialized tool E_{vllm} , built upon a VLLM backbone, to perform high-order cognition and semantic reasoning. Formally, the semantic anomaly analysis is computed as:

$$A_{\text{semantic}} = E_{\text{vllm}}(I \mid \mathcal{G}_{\text{semantic}}). \quad (5)$$

Here, A_{semantic} denotes the structured **Semantic Anomaly Analysis Report**, summarizing AgentFoX’s initial semantic-level assessment and prioritizing anomaly hypotheses that guide the fusion of expert forensic models. $\mathcal{G}_{\text{semantic}}$ denotes the *semantic-analysis guideline*, a purpose-built prompt encoding principled instructions for semantic anomaly detection. Under the constraint of $\mathcal{G}_{\text{semantic}}$, E_{vllm} examines the scene for logical inconsistencies (e.g., impossible spatial layouts), physically implausible effects (e.g., shadows or reflections), anatomical anomalies (e.g., extra fingers), and other semantic-level artifacts indicative of AI-generated imagery.

Stage 2: Signal-level Results Analysis

Building on the semantic overview from Stage 1, AgentFoX conducts fine-grained signal-level forensic analysis using a set of calibrated expert detectors. For the input image I , the agent queries each expert M_j to obtain a raw score p_j . This score is calibrated by the tool-specific function \hat{F}_j^{TOOL} provided in $\mathcal{E}_{\text{expertProfile}}(M_j)$, yielding p'_j . The resulting score pairs $\{p_j, p'_j\}$ are then combined with descriptive metadata $T_{\text{desc},j}^{\text{LLM}}$ and quality metrics $T_{\text{quality},j}^{\text{LLM}}$. Formally,

the aggregated signal-level assessment is:

$$A_{\text{experts}} = \text{LLM}(\{p_j, p'_j, T_{\text{desc},j}^{\text{LLM}}, T_{\text{quality},j}^{\text{LLM}}\}_{j=1}^N \mid \mathcal{G}_{\text{expert}}). \quad (6)$$

Here, A_{experts} is the structured **Signal-level Analysis Report**. It compiles calibrated scores, confidence estimates, and the domain relevance of each expert. $\mathcal{G}_{\text{expert}}$ is the *signal-analysis guideline*, a compact rule set specifying forensic constraints and aggregation principles for heterogeneous expert outputs. To generate A_{experts} , the LLM evaluates the aggregated signal-level findings. It assesses conflicts among expert outputs and determines the degree of trust assigned to each, in alignment with their respective reliability profiles.

Stage 3: Conflict Resolution

This stage is triggered when A_{semantic} and A_{experts} yield mutually contradictory decisions. Upon detecting an explicit conflict, AgentFoX invokes a data-centric reliability evaluation A_{cluster} derived from modality-specific entries in $\mathcal{C}_{\text{clusterProfile}}(t)$, as defined in Stage 2 (cluster-profile analysis). For each modality t , the agent determines its cluster index c via $\{\mathcal{C}_c^{(t)}\}^{\text{TOOL}}$, retrieves the corresponding reliability value $T_{\text{Rc},t}^{\text{LLM}}$ and quality measure $T_{\text{Q},t}^{\text{LLM}}$, and interprets them according to $\mathcal{G}_{\text{cluster}}$:

$$A_{\text{cluster}} = \text{LLM}(T_{\text{Rc},t}^{\text{LLM}}, T_{\text{Q},t}^{\text{LLM}} \mid \mathcal{G}_{\text{cluster}}). \quad (7)$$

Here, A_{cluster} represents the structured data-centric reliability report, summarizing modality-wise reliability and quality characteristics to support subsequent decision adjudication.

When conflicts arise, AgentFoX does not simply rely on linear score aggregation. Instead, it employs **contextual arbitration** A_{arb} : an integrative reasoning process that holistically integrates the full spectrum of available evidence. This includes the semantic findings (A_{semantic}), the signal-level reports (A_{experts}), and the data-centric clustering content (A_{cluster}). The subsequent synthesis of this multifaceted evidence allows the agent to arrive at a conclusion that transcends any single source. **Crucially, mirroring the deliberative, evidence-driven reasoning of a human forensic expert ensures the process is both principled and auditable, inherently mitigating model hallucination.** Every step is traceable to specific information within the provided forensic reports, ensuring the final verdict is a faithful synthesis of the input context.

Stage 4: Forensic Investigation Report

In the final stage, the agent generates a comprehensive **Forensic Report**. This report, denoted as $\text{Report} \triangleq \{V, P\}$, encapsulates both the final verdict V and a detailed provenance trace P . Instead of a single, uncalibrated confidence score, the provenance P offers a transparent, step-by-step justification that makes the entire reasoning process

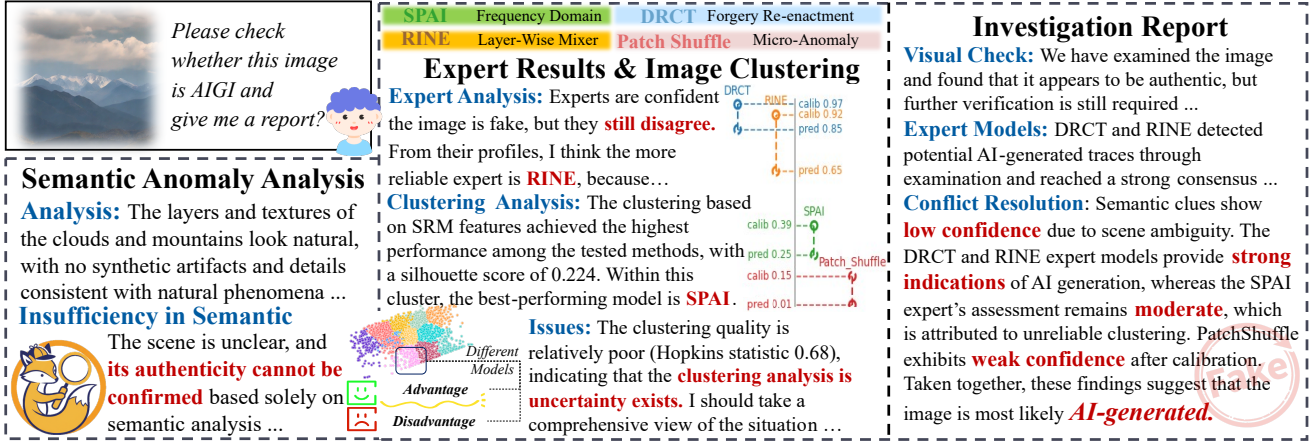


Figure 3. Figure 3 showcases the agent’s reasoning flow. After an ambiguous semantic analysis (Stage 1), it identifies conflicting expert opinions (Stage 2). During conflict resolution (Stage 3), the agent arbitrates by consulting both Expert and Clustering Profiles. Recognizing the cluster’s unreliability, it down-weights this context and trusts the globally more reliable experts. This traceable adjudication culminates in the final report (Stage 4).

auditable. The report is synthesized from a collected evidence set \mathcal{A} under the guidance of $\mathcal{G}_{\text{report}}$:

$$\text{Report} = \text{LLM}(I, \mathcal{A} \mid \mathcal{G}_{\text{report}}). \quad (8)$$

The evidence set \mathcal{A} comprises A_{semantic} and A_{experts} . When a conflict arises and is subsequently resolved, \mathcal{A} is dynamically augmented to include A_{cluster} and A_{arb} . In this context, the role of the LLM is to faithfully synthesize these components into a coherent report, where A_{arb} provides the definitive reasoning for the final verdict. This ensures the report serves as an auditable summary of the decision-making process rather than a re-evaluation of the evidence.

3.3. Quick Integration

AgentFoX adopts a modular architecture supporting *quick integration* of new signal-level expert models with minimal disruption to online inference. When incorporating a new expert detector, the system registers its interface with the Toolkit alongside its *core mechanism* and *primary use cases*. If labeled data is available, a full *Profile Investigation* (Sect. 3.1) can be performed to construct Expert and Clustering Profiles, enabling precise model weighting and conflict resolution in *Agentic Inference* (Sect. 3.2). In scenarios without labeled data, the framework reuses generic or template-based profiles to enable the new expert to immediately participate, with adaptive confidence adjustment to mitigate uncertainty. Removing an expert requires only deleting its interface and associated profile entries. This design reduces integration and maintenance effort, while allowing rapid incorporation of emerging AIGI detectors and agile adaptation to evolving forensic technologies. Fig. 3

illustrates our multi-expert fusion producing a transparent forensic report and final verdict for the input image.

4. Experiments

Unless otherwise noted, the proposed agent uses Qwen3 [40] as its backbone LLM and GPT-4o [28] as the semantic VLLM; for reproducibility, we set the random seed to 42 and the temperature to 0. All detectors are publicly available pre-trained models without further fine-tuning.

4.1. X-Fuse: High-Conflict Benchmark

To evaluate our agent’s capacity to resolve conflicts among diverse expert detectors and integrate heterogeneous AIGI forensic cues, we curate **X-Fuse** — a benchmark assembled from existing public AIGI testsets via stratified sampling, and is deliberately structured to induce maximal inter-detector disagreement. This design yields a controlled, high-conflict environment that serves as a targeted stress test for fusion strategies. We formally define a conflict vector as follows:

$$g(x) = [E_1(x), \dots, E_j(x) \mid GT(x)] \in \{0, 1\}^{j+1} \quad (9)$$

where $E_j(x) = 1$ if detector j misclassifies sample x , and 0 otherwise; $GT(x) = 1$ if x is AIGI, and 0 if it is real. This vector encodes the binary error pattern of all experts alongside the ground-truth label, yielding a fine-grained disagreement signature.

Given j expert detectors, d datasets, and n samples per conflict vector, there are 2^{j+1} possible binary configurations of $g(x)$, covering every expert-error/ground-truth

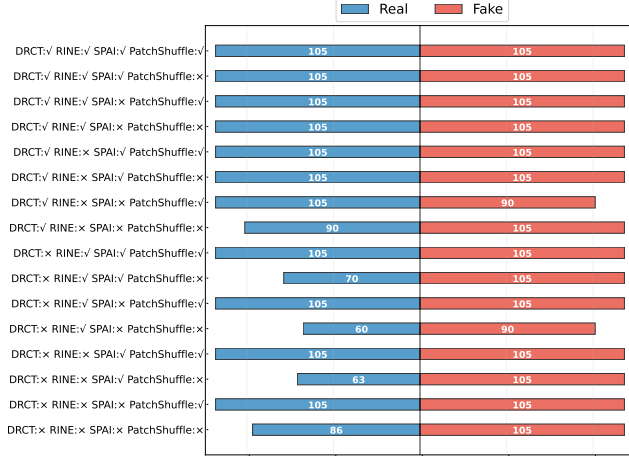


Figure 4. Sample sizes and cross-domain distribution for the decision-label-generator grouping. Some cells did not meet the target quota of 7×15 due to limited global availability.

combination. The target benchmark size is:

$$N_{\text{target}}(j, d, n) = 2^{j+1} \cdot d \cdot n \quad (10)$$

We set $j = 4$ (DRCT [2], RINE [15], SPAI [13], Patch Shuffle [45]), $d = 7$ (GenImage [49], AIGCDetect [46], AIGIBench [19], Chameleon [38], Community Forensic [29], WIRA [24], WildFake [10]), and $n = 15$ to balance coverage and sample availability.

Substituting values yields $N_{\text{target}} = 3,360$, with the realized benchmark containing 3,174 samples (94.5% coverage); underpopulated cells are proportionally filled from remaining datasets (Fig.4). This stratification increases inter-expert disagreement, drives individual expert accuracy toward 0.5, and produces a challenging adversarial benchmark for evaluating agent-based fusion under realistic AIGI conditions.

Additionally, we sample 4,800 images from the GenImage [49] training split (150 per $g(x)$ cell), partitioned into 80% used for calibration, clustering, and aggregation models, with the remaining 20% reserved for profile generation and model selection. Notably, X-Fuse is assembled from the official test splits of seven public datasets and hash-deduplicated to ensure **no overlap** with any training or profile data.

4.2. Robustness to Expert Disagreement

As shown in Table 1, each cell presents F1-Score (left) and Accuracy (acc, right) computed at a fixed threshold of 0.5, with **bold** indicating the best and underlined indicating the second-best results, respectively. We compare four aggregation paradigms on the constructed high-conflict benchmark:

- **Multifaceted Experts:** Four signal-level detectors (DRCT [2], RINE [15], SPAI [13], Patch Shuffle [45]) and one semantic-level VLLM analyzer [28].

- **Parameter-Agnostic:** Majority Vote aggregates five expert decisions; Probability Average computes weighted averages of output probabilities.
- **Learnable Fusion:** Gating Network learns weights over 2^4 expert combinations; ResNet Fusion retrains only the classification head; MLP Fusion trains an MLP on concatenated penultimate-layer features. All trained for 10 epochs with identical settings; best checkpoints selected via validation accuracy.
- **Existing SOTA:** C2P-CLIP [34] and DeeCLIP [14] rely on signal-level detection, whereas FakeVLM [36] is a semantic-level detector based on MLLM. Our evaluation focuses on their generalization performance across challenging high-conflict benchmark (X-Fuse) and multiple real-world datasets.

Experiments on our **X-Fuse** benchmark confirm the superiority of AgentFoX in challenging zero-shot cross-domain scenarios with conflicting signals (Table 1). At its core, an LLM agent intelligently arbitrates between the outputs of heterogeneous experts to resolve contradictions. This arbitration is key to preventing overfitting to any single expert’s bias, thus enabling robust generalization to unseen domains without the need for fine-tuning.

We analyzed AgentFoX’s performance over 16 stratified expert-decision combinations with varying degrees of disagreement (Fig. 5). Results show a clear negative correlation between conflict intensity—driven by weaker-expert dominance and cross-domain feature divergence—and detection accuracy. The method approaches perfect performance in low-conflict settings, degrades in a controlled, step-wise manner under moderate conflicts, and retains non-trivial accuracy even in extreme cases with systematic expert disagreement. These observations indicate that the proposed LLM-driven conflict-resolution mechanism sustains useful detection capability across varying conflict levels.

4.3. In-the-Wild Evaluation

We assess in-the-wild generalization on two complementary yet challenging datasets: WildFake [10], comprising AI-generated and authentic social media imagery, and WIRA [24], containing paired authentic and synthetic images. Both datasets are collected from real-world online environments and exhibit markedly different performance characteristics, with methods that excel on one often experiencing sharp performance drops on the other.

Using the official implementations of leading baselines, including the strongest single-model and ensemble detectors, we show that our agent-based fusion consistently achieves the highest accuracy on both datasets and delivers notable gains over the best individual and aggregated models. This robustness stems from our adaptive reweighting mechanism, which detects each expert’s weaknesses under

Table 1. Performance of cross-domain AI-generated image detection in high-conflict multi-expert setting (**X-Fuse**). We compare single experts, parameter-free aggregation, trainable fusion, and our proposed method on the benchmark. Metrics show F1/ACC (left/right; **bold**=best, underline=second-best); computed at threshold=0.5; "Overall" aggregates all samples.

Model	GenImage[49]	AIGCDetect[46]	AIGIBench[19]	Chameleon[38]	Community Forensics[29]	WIRA[24]	WildFake[10]	Overall
DRCT[2]	0.5133/0.5353	0.4576/0.4787	0.5396/0.5233	0.4383/0.4626	0.6127/0.5499	0.5824/0.6056	0.5634/0.5401	0.5198/0.5198
RINE[15]	0.5138/0.5176	0.4607/0.4645	0.5792/0.5876	0.4055/0.4243	0.6329/0.5670	0.6551/0.6694	0.4903/0.5312	0.5223/0.5246
SPAI[13]	0.5019/0.4824	0.4629/0.4610	0.5383/0.5055	0.4348/0.4809	0.6441/0.5812	0.4345/0.4722	0.5850/0.5579	0.5094/0.4994
Patch Shuffle[45]	0.4930/0.5000	0.4584/0.4805	0.5145/0.4812	0.4389/0.4725	0.5905/0.5100	0.5429/0.5556	0.6410/0.5846	0.5168/0.5050
Semantic Analyzer [28]	0.6585/0.7255	0.6303/0.7358	<u>0.8465/0.8448</u>	<u>0.6699/0.7754</u>	0.7767/0.7265	0.1749/0.5806	0.9073/0.8902	0.7108/0.7549
Majority Vote*	0.5751/0.6118	0.5070/0.5621	0.6771/0.6785	0.4500/0.5241	0.7012/0.6553	0.5594/0.6500	0.7283/0.7211	0.5822/0.6166
Probability Avg*	0.6780/0.7039	0.5873/0.6312	0.7336/0.7295	0.5214/0.5907	0.7552/0.7009	0.6345/0.7056	0.8095/0.7864	0.6680/0.6818
Gating Network	0.6118/0.6236	0.5319/0.5269	0.5122/0.5154	0.4459/0.4188	0.5954/0.6553	0.6222/0.6114	0.5994/0.6197	0.5501/0.5576
Resnet Fusion	0.9478/0.9465	0.7075/0.7315	0.4926/0.6060	0.3388/0.6506	0.7337/0.6864	0.6691/0.7500	0.5302/0.5870	0.6428/0.7197
MLP Fusion	<u>0.9353/0.9359</u>	<u>0.7067/0.7262</u>	0.6075/0.4840	0.6522/0.3056	0.8494/0.7949	<u>0.7306/0.6255</u>	0.6142/0.5667	0.6608/0.7221
C2P-CLIP[34]	0.7399/0.7863	0.7308/0.8014	0.2230/0.4900	0.0760/0.5957	0.5210/0.5128	0.1808/0.5972	0.4718/0.5549	0.4756/0.6345
DeeCLIP[14]	0.6045/0.6922	0.6634/0.7589	0.3026/0.5299	0.0920/0.6057	0.5989/0.5726	0.2488/0.5472	0.5581/0.6053	0.4739/0.6257
FakeVLM [36]	0.1219/0.5196	0.1677/0.5426	0.7284/0.6231	0.6744/0.6256	0.4134/0.4501	0.2727/0.6000	0.7513/0.7151	0.5278/0.5807
AgentFoX-8B	0.7336/0.7294	0.6593/0.6702	0.8267/0.7978	0.6595/0.6839	0.8494/0.7949	0.5664/0.6556	0.8883/0.8627	0.7451/0.7329
AgentFoX-32B	0.7854/0.7804	0.7558/0.7571	0.8975/0.8825	0.6914/0.7088	0.9150/0.8803	0.7323/0.7583	0.8921/0.8665	0.8087/0.7949

Table 2. In-the-Wild Generalization: Detection Evaluation on Real-World WIRA and WildFake

	WIRA (All)		WildFake (All)		Overall	
	F1	ACC	F1	ACC	F1	ACC
DRCT [2]	0.9377	0.9374	0.6962	0.7180	<u>0.8559</u>	<u>0.8592</u>
RINE [15]	0.6234	0.7015	0.6220	0.6930	0.6229	0.6985
PatchShuffle [45]	<u>0.9555</u>	<u>0.9552</u>	0.3867	0.5881	0.8019	0.8243
SPAI [13]	0.8581	0.8529	0.8084	0.7889	0.8397	0.8301
Semantic Analyzer [28]	0.1333	0.5274	<u>0.9074</u>	<u>0.9090</u>	0.5201	0.6635
Gating Network	0.8807	0.8833	0.7156	0.7425	0.8248	0.8331
ResNet Fusion	0.8498	0.8633	0.5263	0.6497	0.7493	0.7871
MLP Fusion	0.8572	0.8684	0.5719	0.6693	0.7667	0.7975
C2P-CLIP [34]	0.1422	0.5289	0.5133	0.6243	0.3047	0.5629
DeeCLIP [14]	0.3002	0.5643	0.5352	0.6551	0.3937	0.5967
FakeVLM [36]	0.2927	0.5638	0.7342	0.7153	0.5092	0.6178
AgentFoX-32B	0.9579	0.9575	0.9326	0.9313	0.9488	0.9481

distribution shifts and selectively amplifies their strengths, enabling stable cross-domain performance without sacrificing per-dataset precision.

4.4. Ablation Study

Our method supports **quick integration** of new expert detectors, and ablation results (Table 3) show that the single-expert setting is limited, while detection performance improves consistently as additional experts are incorporated—without requiring any retraining in the fusion stage.

Table 4 shows that removing either **Expert Profiles** or **Clustering Profiles** consistently reduces F1 and ACC. Using only Clustering Profiles outperforms Expert Profiles alone, indicating a stronger impact of context-specific adaptation. The best performance occurs when both modules are combined, confirming the complementarity of global calibration priors and context-aware weighting. Even without

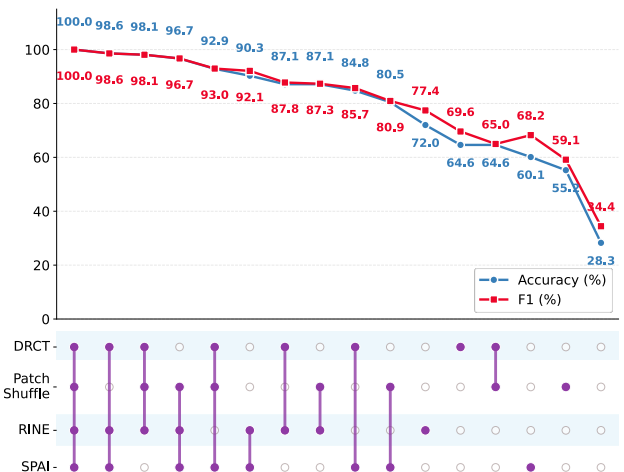


Figure 5. Accuracy and F1-Score of the proposed agentic aggregation method across 16 expert-decision combinations with varying conflict intensities. The upper panel shows performance metrics (blue solid circles and purple dashed squares); the lower panel shows the corresponding signal-level expert composition.

Table 3. Ablation Study on Expert Integration: Detection performance improves as additional experts (RINE [15], PatchShuffle [45], SPAI [13], DRCT [2]) are registered via profiling without fusion-stage retraining.

RINE	PatchShuffle	SPAI	DRCT	F1	ACC
✓				0.5737	0.6070
✓	✓			0.6617	0.6830
✓	✓	✓		0.7282	0.6846
✓	✓	✓	✓	0.8087	0.7949

profile information, our agent-guided fusion still exceeds most standalone SOTA detectors on X-Fuse (cf. Table 1).

Table 4. Ablation study on the effect of Expert Profiles and Clustering Profiles for AI-generated image detection. Results are reported in terms of F1 and ACC.

Expert Profiles	Clustering Profiles	F1	ACC
✗	✗	0.7032	0.6738
✓	✗	0.7177	0.6836
✗	✓	0.7597	0.7376
✓	✓	0.8087	0.7949

5. Conclusion

In this paper, we present **AgentFoX**, a framework addressing the challenge of reconciling conflicting predictions among heterogeneous, specialized AIGI detectors. Guided by an offline knowledge base comprising calibrated **Expert Profiles** and contextual **Clustering Profiles**, an LLM agent performs dynamic, multi-stage reasoning to adjudicate expert opinions within a structured, human-like workflow. Our approach achieves competitive or superior detection accuracy compared to prior state-of-the-art methods, while enhancing interpretability through explainable, multifaceted forensic reports. Its quick integration capability—requiring no retraining in the fusion stage—facilitates scalable real-world deployment and rapid incorporation of newly emerging detectors.

Ultimately, **AgentFoX** demonstrates that agent-driven multi-expert fusion, when coupled with offline profiling, can serve as a robust and adaptable paradigm for digital forensics. We envision its use in continuously evolving ecosystems of forensic tools, enabling trustworthy and resilient systems capable of keeping pace with the rapid advancement of AI-generated content.

References

- [1] Adil M Bagirov, Ramiz M Aliguliyev, and Nargiz Sultanova. Finding compact and well-separated clusters: Clustering using silhouette coefficients. *Pattern Recognition*, 135:109144, 2023. 4
- [2] Baoying Chen, Jishen Zeng, Jianquan Yang, and Rui Yang. Drct: diffusion reconstruction contrastive training towards universal detection of diffusion generated images. In *Proceedings of the 41st International Conference on Machine Learning*. JMLR.org, 2024. 1, 7, 8
- [3] Ruoxin Chen, Junwei Xi, Zhiyuan Yan, Ke-Yue Zhang, Shuang Wu, Jingyi Xie, Xu Chen, Lei Xu, Isabel Guan, Taiping Yao, et al. Dual data alignment makes ai-generated image detector easier generalizable. *arXiv preprint arXiv:2505.14359*, 2025. 2
- [4] Yize Chen, Zhiyuan Yan, Guangliang Cheng, Kangran Zhao, Siwei Lyu, and Baoyuan Wu. X2-dfd: A framework for explainable and extendable deepfake detection. *arXiv preprint arXiv:2410.06126*, 2024. 2
- [5] David L. Davies and Donald W. Bouldin. A cluster separation measure. *IEEE Transactions on Pattern Analysis and Machine Intelligence*, PAMI-1(2):224–227, 1979. 4
- [6] Jessica Fridrich and Jan Kodovsky. Rich models for steganalysis of digital images. *IEEE Transactions on Information Forensics and Security*, 7(3):868–882, 2012. 4
- [7] W Brier Glenn et al. Verification of forecasts expressed in terms of probability. *Monthly weather review*, 78(1):1–3, 1950. 4
- [8] Fabrizio Guillaro, Giada Zingarini, Ben Usman, Avneesh Sud, Davide Cozzolino, and Luisa Verdoliva. A bias-free training paradigm for more general ai-generated image detection. In *Proceedings of the Computer Vision and Pattern Recognition Conference*, pages 18685–18694, 2025. 2
- [9] Chuan Guo, Geoff Pleiss, Yu Sun, and Kilian Q Weinberger. On calibration of modern neural networks. In *International conference on machine learning*, pages 1321–1330. PMLR, 2017. 4
- [10] Yan Hong and Jianfu Zhang. Wildfake: A large-scale challenging dataset for ai-generated images detection. *arXiv preprint arXiv:2402.11843*, 2024. 7, 8
- [11] Qing Huang, Zhipei Xu, Xuanyu Zhang, and Jian Zhang. UniShield: An adaptive multi-agent framework for unified forgery image detection and localization, 2025. 3
- [12] Yikun Ji, Hong Yan, Jun Lan, Huijia Zhu, Weiqiang Wang, Qi Fan, Liqing Zhang, and Jianfu Zhang. Interpretable and reliable detection of ai-generated images via grounded reasoning in mllms. *arXiv preprint arXiv:2506.07045*, 2025. 2
- [13] Dimitrios Karageorgiou, Symeon Papadopoulos, Ioannis Kompatsiaris, and Efstratios Gavves. Any-resolution ai-generated image detection by spectral learning. In *Proceedings of the Computer Vision and Pattern Recognition Conference*, pages 18706–18717, 2025. 1, 7, 8
- [14] Mamadou Keita, Wassim Hamidouche, Hessen Bougueffa Eutamene, Abdelmalik Taleb-Ahmed, and Abdenour Hadid. Deeclip: A robust and generalizable transformer-based framework for detecting ai-generated images. *arXiv preprint arXiv:2504.19876*, 2025. 7, 8
- [15] Christos Koutlis and Symeon Papadopoulos. Leveraging representations from intermediate encoder-blocks for synthetic image detection. In *European Conference on Computer Vision*, pages 394–411. Springer, 2024. 1, 2, 7, 8
- [16] Meelis Kull, Telmo Silva Filho, and Peter Flach. Beta calibration: a well-founded and easily implemented improvement on logistic calibration for binary classifiers. In *Artificial intelligence and statistics*, pages 623–631. PMLR, 2017. 4
- [17] Yingxin Lai, Zitong Yu, Jun Wang, Linlin Shen, Yong Xu, and Xiaochun Cao. Agent4FaceForgery: Multi-agent LLM framework for realistic face forgery detection, 2025. 3
- [18] Chunxiao Li, Xiaoxiao Wang, Meiling Li, Boming Miao, Peng Sun, Yunjian Zhang, Xiangyang Ji, and Yao Zhu. Bridging the gap between ideal and real-world evaluation: Benchmarking ai-generated image detection in challenging scenarios. In *Proceedings of the IEEE/CVF International Conference on Computer Vision*, pages 20379–20389, 2025. 3

- [19] Ziqiang Li, Jiazhen Yan, Ziwen He, Kai Zeng, Weiwei Jiang, Lizhi Xiong, and Zhangjie Fu. Is artificial intelligence generated image detection a solved problem? *arXiv preprint arXiv:2505.12335*, 2025. 7, 8
- [20] Kaiqing Lin, Yuzhen Lin, Weixiang Li, Taiping Yao, and Bin Li. Standing on the shoulders of giants: Reprogramming visual-language model for general deepfake detection. In *Proceedings of the AAAI Conference on Artificial Intelligence*, pages 5262–5270, 2025. 2
- [21] Kaiqing Lin, Zhiyuan Yan, Ruoxin Chen, Junyan Ye, Ke-Yue Zhang, Yue Zhou, Peng Jin, Bin Li, Taiping Yao, and Shouhong Ding. Seeing before reasoning: A unified framework for generalizable and explainable fake image detection. *arXiv preprint arXiv:2509.25502*, 2025. 2
- [22] Huan Liu, Zichang Tan, Chuangchuang Tan, Yunchao Wei, Jingdong Wang, and Yao Zhao. Forgery-aware adaptive transformer for generalizable synthetic image detection. In *Proceedings of the IEEE/CVF Conference on Computer Vision and Pattern Recognition*, pages 10770–10780, 2024. 2, 12, 13
- [23] Rastislav Lukac and Konstantinos N Plataniotis. Color filter arrays: Design and performance analysis. *IEEE Transactions on Consumer electronics*, 51(4):1260–1267, 2005. 4
- [24] Andrew McDonald. What is real anymore? an ai/ml image dataset using authenticity validation and traceable origins for every data instance. In *Workshop on Datasets and Evaluators of AI Safety*, 2025. 7, 8
- [25] Alexandru Niculescu-Mizil and Rich Caruana. Predicting good probabilities with supervised learning. In *Proceedings of the 22nd International Conference on Machine Learning*, page 625–632, New York, NY, USA, 2005. Association for Computing Machinery. 4
- [26] Jeremy Nixon, Michael W Dusenberry, Linchuan Zhang, Ghassen Jerfel, and Dustin Tran. Measuring calibration in deep learning. In *CVPR workshops*, 2019. 4
- [27] Utkarsh Ojha, Yuheng Li, and Yong Jae Lee. Towards universal fake image detectors that generalize across generative models. In *Proceedings of the IEEE/CVF Conference on Computer Vision and Pattern Recognition*, pages 24480–24489, 2023. 12, 13
- [28] OpenAI. Gpt-4o system card, 2024. 6, 7, 8
- [29] Jeongsoo Park and Andrew Owens. Community forensics: Using thousands of generators to train fake image detectors. In *Proceedings of the Computer Vision and Pattern Recognition Conference*, pages 8245–8257, 2025. 7, 8
- [30] John Platt et al. Probabilistic outputs for support vector machines and comparisons to regularized likelihood methods. *Advances in large margin classifiers*, 10(3):61–74, 1999. 4
- [31] Alec Radford, Jong Wook Kim, Chris Hallacy, Aditya Ramesh, Gabriel Goh, Sandhini Agarwal, Girish Sastry, Amanda Askell, Pamela Mishkin, Jack Clark, et al. Learning transferable visual models from natural language supervision. In *International conference on machine learning*, pages 8748–8763. PmLR, 2021. 4
- [32] Chuangchuang Tan, Yao Zhao, Shikui Wei, Guanghua Gu, Ping Liu, and Yunchao Wei. Frequency-aware deepfake detection: improving generalizability through frequency space domain learning. In *Proceedings of the Thirty-Eighth AAAI Conference on Artificial Intelligence and Thirty-Sixth Conference on Innovative Applications of Artificial Intelligence and Fourteenth Symposium on Educational Advances in Artificial Intelligence*. AAAI Press, 2024. 12, 13
- [33] Chuangchuang Tan, Yao Zhao, Shikui Wei, Guanghua Gu, Ping Liu, and Yunchao Wei. Rethinking the up-sampling operations in cnn-based generative network for generalizable deepfake detection. In *Proceedings of the IEEE/CVF Conference on Computer Vision and Pattern Recognition*, pages 28130–28139, 2024. 12, 13
- [34] Chuangchuang Tan, Renshuai Tao, Huan Liu, Guanghua Gu, Baoyuan Wu, Yao Zhao, and Yunchao Wei. C2p-clip: Injecting category common prompt in clip to enhance generalization in deepfake detection. In *Proceedings of the AAAI Conference on Artificial Intelligence*, pages 7184–7192, 2025. 2, 7, 8
- [35] Sheng-Yu Wang, Oliver Wang, Richard Zhang, Andrew Owens, and Alexei A Efros. Cnn-generated images are surprisingly easy to spot... for now. In *Proceedings of the IEEE/CVF conference on computer vision and pattern recognition*, pages 8695–8704, 2020. 2
- [36] Siwei Wen, Junyan Ye, Peilin Feng, Hengrui Kang, Zichen Wen, Yize Chen, Jiang Wu, Wenjun Wu, Conghui He, and Weijia Li. Spot the fake: Large multimodal model-based synthetic image detection with artifact explanation. *arXiv preprint arXiv:2503.14905*, 2025. 2, 5, 7, 8
- [37] Zhipei Xu, Xuanyu Zhang, Xing Zhou, and Jian Zhang. Avatarshield: Visual reinforcement learning for human-centric video forgery detection. *arXiv preprint arXiv:2505.15173*, 2025. 2, 5
- [38] Shilin Yan, Ouxiang Li, Jiayin Cai, Yanbin Hao, Xiaolong Jiang, Yao Hu, and Weidi Xie. A sanity check for ai-generated image detection. *arXiv preprint arXiv:2406.19435*, 2024. 7, 8
- [39] Zhiyuan Yan, Jiangming Wang, Peng Jin, Ke-Yue Zhang, Chengchun Liu, Shen Chen, Taiping Yao, Shouhong Ding, Baoyuan Wu, and Li Yuan. Orthogonal subspace decomposition for generalizable AI-generated image detection. In *Forty-second International Conference on Machine Learning*, 2025. 2
- [40] An Yang, Anfeng Li, Baosong Yang, Beichen Zhang, Binyuan Hui, Bo Zheng, Bowen Yu, Chang Gao, Chengen Huang, Chenxu Lv, et al. Qwen3 technical report. *arXiv preprint arXiv:2505.09388*, 2025. 6
- [41] Shunyu Yao, Jeffrey Zhao, Dian Yu, Nan Du, Izhak Shafran, Karthik R Narasimhan, and Yuan Cao. React: Synergizing reasoning and acting in language models. In *The eleventh international conference on learning representations*, 2022. 3
- [42] Nikolaos-Antonios Ypsilantis, Kaifeng Chen, Bingyi Cao, Mário Lipovský, Pelin Dogan-Schönberger, Grzegorz Makosa, Boris Bluntschli, Mojtaba Seyedhosseini, Ondřej Chum, and André Araujo. Towards universal image embeddings: A large-scale dataset and challenge for generic image representations. In *Proceedings of the IEEE/CVF International Conference on Computer Vision*, pages 11290–11301, 2023. 2

- [43] Bianca Zadrozny and Charles Elkan. Obtaining calibrated probability estimates from decision trees and naive bayesian classifiers. In *Icml*, 2001. 4
- [44] Wayne Zhang, Changjiang Jiang, Zhonghao Zhang, Chenyang Si, Fengchang Yu, and Wei Peng. Ivy-fake: A unified explainable framework and benchmark for image and video aigc detection. *arXiv preprint arXiv:2506.00979*, 2025. 2, 5
- [45] Chende Zheng, Chenhao Lin, Zhengyu Zhao, Hang Wang, Xu Guo, Shuai Liu, and Chao Shen. Breaking semantic artifacts for generalized ai-generated image detection. *Advances in Neural Information Processing Systems*, 37:59570–59596, 2024. 1, 7, 8
- [46] Nan Zhong, Yiran Xu, Sheng Li, Zhenxing Qian, and Xinpeng Zhang. Patchcraft: Exploring texture patch for efficient ai-generated image detection. *arXiv preprint arXiv:2311.12397*, 2023. 7, 8
- [47] Yue Zhou, Xinan He, KaiQing Lin, Bin Fan, Feng Ding, and Bin Li. Breaking latent prior bias in detectors for generalizable aigc image detection. *arXiv preprint arXiv:2506.00874*, 2025. 2
- [48] Ziyin Zhou, Yunpeng Luo, Yuanchen Wu, Ke Sun, Jiayi Ji, Ke Yan, Shouhong Ding, Xiaoshuai Sun, Yunsheng Wu, and Rongrong Ji. Aigi-holmes: Towards explainable and generalizable ai-generated image detection via multimodal large language models. *arXiv preprint arXiv:2507.02664*, 2025. 2, 3
- [49] Mingjian Zhu, Hanting Chen, Qiangyu Yan, Xudong Huang, Guanyu Lin, Wei Li, Zhijun Tu, Hailin Hu, Jie Hu, and Yunhe Wang. Genimage: a million-scale benchmark for detecting ai-generated image. In *Proceedings of the 37th International Conference on Neural Information Processing Systems*, Red Hook, NY, USA, 2023. Curran Associates Inc. 7, 8



AgentFoX: LLM Agent-Guided Fusion with eXplainability for AI-Generated Image Detection

Supplementary Material

A. Extended Benchmark Evaluation

We extend the empirical evaluation in the main paper by comparing AgentFoX with four additional standalone AIGI detectors: FatFormer [22], NPR [33], FreqNet [32], and UniFD [27]. Because these methods are evaluated as standalone systems rather than as components within AgentFoX, they serve as external baselines for assessing whether the proposed agent-guided fusion strategy offers benefits beyond individual detectors.

We report two complementary evaluation settings. Table 5 summarizes results under the unified X-Fuse sampling protocol, where the seven source datasets are re-sampled to form a high-conflict benchmark. Table 6 instead reports dedicated in-the-wild evaluations on WIRA and WildFake under a different sampling protocol. The WIRA and WildFake results in these two tables are therefore provided only as complementary references and are not intended for direct comparison. For conciseness, Table 6 reports only AgentFoX-32B, the final model used in the main paper.

Under the X-Fuse protocol, AgentFoX-32B achieves the best overall F1 and accuracy, outperforming all standalone baselines by a clear margin. Under the separate in-the-wild protocol, AgentFoX again delivers the strongest performance across all reported metrics. Overall, these results suggest that the gains of AgentFoX are not solely attributable to access to multiple detector outputs; rather, explicit reasoning over complementary and often conflicting forensic evidence appears to play an important role.

B. Additional Analyses

We provide four complementary analyses—seed stability, clustering-profile construction, robustness under JPEG compression, and inference cost—followed by representative failure cases and examples of the knowledge structures supplied to the agent. Together, these additions further characterize AgentFoX beyond the results reported in the main paper.

B.1. Seed Stability

The primary source of nondeterminism in AgentFoX is LLM decoding. To verify that this stochasticity rarely changes the final verdict, we evaluate AgentFoX-32B using three random seeds and report both aggregate performance and sample-level prediction consistency. In addition to F1 and accuracy, we measure pairwise agreement across seeds

and the proportion of samples whose predicted labels remain identical in all three runs. As shown in Table 7, performance varies only slightly across seeds, while sample-level consistency remains high, indicating that stochastic decoding rarely changes the final verdict.

B.2. Construction of Clustering Profiles

The Clustering Profiles provide context-dependent estimates of expert reliability on a per-image basis. For each image, we extract features from three complementary modalities:

- **CLIP (semantic):** 768-dimensional embeddings from a CLIP ViT-L/14 model fine-tuned for AIGI detection.
- **SRM (texture):** responses from 30 SRM high-pass filters, aggregated into a 34-dimensional GLCM-based descriptor.
- **CFA (camera artifacts):** a 64-dimensional descriptor combining statistical, spatial, and FFT-based frequency attributes.

Each modality is clustered independently using K-means on the reference split used for profile construction. The number of clusters K is selected from the elbow of the inertia curve using the peak second derivative, yielding $K = 12$ for CLIP, $K = 8$ for SRM, and $K = 10$ for CFA. At inference time, each image is assigned to its nearest cluster in each modality, and the corresponding reliability statistics are provided to the agent as Clustering Profiles.

B.3. Robustness under JPEG Compression

JPEG compression attenuates the high-frequency traces on which many signal-level detectors rely. To assess robustness, we evaluate performance across a range of compression quality factors. Figure 6 shows that AgentFoX retains comparatively strong accuracy even under severe compression. This trend is consistent with the design of AgentFoX, which allows the agent to reduce reliance on perturbation-sensitive experts and place greater emphasis on cues that remain stable under compression. The resulting robustness is therefore consistent with the intended effect of profile-guided arbitration.

B.4. Inference Cost and Performance

Compared with single-expert pipelines and lightweight semantic baselines, AgentFoX-32B incurs substantially higher end-to-end inference cost, requiring on average 15.9 seconds per image and approximately 6.8k total tokens per sample (Table 8). Here, the token count denotes the total

Table 5. Extended benchmark results on the **X-Fuse** dataset under the X-Fuse sampling protocol. Each entry reports F1 / ACC, following the metric definitions used in the main paper. “Overall” denotes the macro-average across the seven source datasets. The WIRA and WildFake columns here correspond to evaluations under the X-Fuse protocol and are not directly comparable to the dedicated in-the-wild results in Table 6. Best and second-best results are shown in **bold** and underlined, respectively; ties are marked jointly.

Model	GenImage	AIGCDetect	AIGIBench	Chameleon	Community Forensics	WIRA (X-Fuse)	WildFake (X-Fuse)	Overall
FatFormer [22]	0.6384/0.7157	0.7453/ 0.8085	0.3301/0.5420	0.1752/0.6246	0.5410/0.5227	0.5232/0.5740	0.3262/0.5639	0.4685/0.6216
NPR [33]	<u>0.7642/0.7725</u>	0.7715/0.7837	0.5722/0.6386	0.3943/0.6473	<u>0.8696/0.8205</u>	<u>0.5798/0.6172</u>	0.2315/0.5389	0.5976/0.6741
FreqNet [32]	0.7348/0.7608	<u>0.7289/0.7837</u>	0.3975/0.5698	0.3061/0.6606	0.6348/0.5869	0.4225/0.5134	0.5214/0.6278	0.5637/0.6582
UniFD [27]	0.5013/0.6294	0.5305/0.6862	0.3077/0.5211	0.1300/0.5990	0.4144/0.4444	0.5013/0.4866	0.2326/0.4500	0.3900/0.5624
AgentFoX-8B	0.7336/0.7294	0.6593/0.6702	<u>0.8267/0.7978</u>	0.6595/0.6839	0.8494/0.7949	0.5664/0.6556	0.8883/0.8627	0.7451/0.7329
AgentFoX-32B	0.7854/0.7804	<u>0.7558/0.7571</u>	0.8975/0.8825	0.6914/0.7088	0.9150/0.8803	0.7323/0.7583	0.8921/0.8665	0.8087/0.7949

Table 6. In-the-wild results on **WIRA** and **WildFake** under a sampling protocol different from that used in X-Fuse. “All” denotes the full evaluation setting under this protocol, and “Overall” denotes the macro-average across the two datasets. These results are provided as complementary references and are not directly comparable to the WIRA/WildFake columns in Table 5. Best and second-best results are shown in **bold** and underlined, respectively.

Model	WIRA (All)		WildFake (All)		Overall	
	F1	ACC	F1	ACC	F1	ACC
FatFormer [22]	0.3400	0.5507	0.4907	0.6231	0.4154	0.5869
NPR [33]	0.1958	0.4901	0.5057	<u>0.6292</u>	0.3508	0.5597
FreqNet [32]	0.4065	<u>0.5765</u>	<u>0.5476</u>	0.6180	<u>0.5026</u>	<u>0.6032</u>
UniFD [27]	<u>0.4828</u>	0.5582	0.2951	0.5181	0.3719	0.5324
AgentFoX-32B	0.9579	0.9575	0.9326	0.9313	0.9488	0.9481

Table 7. Seed stability evaluation on X-Fuse. Besides aggregate F1 and accuracy, we report sample-level prediction consistency across three random seeds. “Pairwise Agreement” is the mean percentage of samples receiving identical predicted labels across seed pairs, and “Unanimous Consistency” is the percentage of samples whose predicted labels are identical in all three runs. High agreement and low variance indicate that stochastic decoding rarely changes the final verdict.

Seed	F1-Score	Accuracy
42	0.8087	0.7949
123	0.7956	0.7944
2024	0.8223	0.8022
Mean ± Std.	0.809 ± 0.013	0.797 ± 0.004

number of input and output tokens consumed by the full pipeline, including expert inference and final-agent reasoning. This overhead reflects the complete multi-stage workflow, including evidence gathering, calibration-aware comparison, conflict resolution, and report generation. In return, AgentFoX substantially improves accuracy on X-Fuse (79.5% vs. roughly 51% for the baseline pipelines) while also producing a structured and auditable forensic report. In high-stakes applications such as misinformation screening

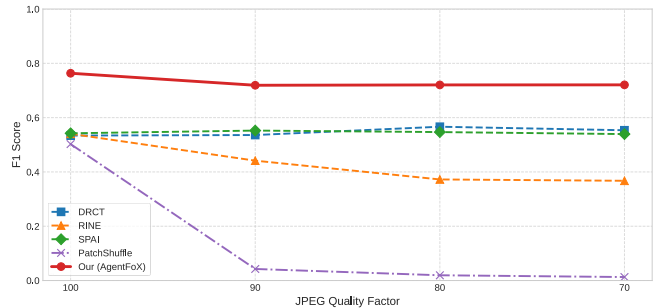


Figure 6. **Robustness under JPEG compression.** AgentFoX maintains strong detection accuracy across a wide range of compression levels, consistent with its ability to adaptively rely more on experts that remain stable under perturbation.

Table 8. **Average end-to-end inference cost and performance** on the X-Fuse benchmark. Time is reported per image for the full pipeline. Token counts denote the total number of input and output tokens consumed per sample, including expert inference and final-agent reasoning. “Signal Experts” denotes direct use of the underlying signal-level detectors without agent-based reasoning or report generation. Although AgentFoX incurs higher latency, it delivers substantially stronger performance and produces a structured forensic report.

Method	Time	Tokens	Acc
Signal Experts	<1s	N/A	51.2%
FakeVLM	4.7s	~0.7k	50.9%
AgentFoX-32B	15.9s	~6.8k	79.5%

and forensic investigation, this additional cost may be acceptable when accuracy and auditability are prioritized over throughput.

B.5. Representative Failure Cases

Figure 7 presents two representative failure cases for AgentFoX. The left example is a real image misclassified as fake, whereas the right example is a fake image misclassified as real. These examples illustrate two representative failure modes observed in our qualitative inspection: misleading signals from imperfect underlying experts and occasional reasoning drift in long-context settings. They help explain

the remaining gap between strong average performance and fully reliable decision-making on especially difficult samples.



Figure 7. **Representative failure cases.** Left: a real image misclassified as fake. Right: a fake image misclassified as real. These examples illustrate two representative failure modes: dependence on imperfect underlying experts and occasional reasoning drift in long-context settings.

In the left false-positive case, misleading artifact cues from several underlying experts dominate the evidence aggregation and push the agent toward an incorrect fake prediction. In the right false-negative case, the agent underweights early warning signals after a long reasoning chain, illustrating a typical instance of reasoning drift. These examples complement the quantitative results and motivate the discussion in Section D.

B.6. Representative Knowledge Structures

To make the agent inputs more concrete, we also provide representative examples of the two main knowledge structures supplied to AgentFoX. Figure 8 shows an example *Expert Profile*, and Figure 9 shows an example SRM-based *Clustering Profile*.

C. Qualitative Reasoning Traces

To illustrate how AgentFoX reaches a final verdict, we present the reasoning protocol together with a representative case study. Figure 10 shows the *Forensic Guideline*, i.e., the rule-based system prompt that structures the agent’s multi-stage reasoning process. Figure 11 then provides a detailed reasoning trace for a challenging AI-generated image that follows this protocol step by step. Together, these examples make the framework’s decision process more transparent and interpretable.

D. Limitations and Future Directions

AgentFoX has two conceptual limitations and one practical one. First, the framework remains fundamentally constrained by the quality of its underlying experts: when the detectors collectively fail to extract meaningful forensic traces from an image—for example, on heavily degraded or out-of-distribution samples—the agent lacks sufficient evidence to produce a reliable verdict. Second, long reasoning chains can diffuse attention away from early but critical expert evidence, occasionally leading to reasoning drift. Al-

though the Forensic Guideline in Figure 10 mitigates this issue to some extent, it remains an open challenge for current LLM-based agents. Third, as quantified in Table 8, the full multi-stage pipeline incurs nontrivial latency and token cost, which may limit deployment in real-time or large-scale screening settings.

Addressing the first limitation requires improving the coverage and robustness of individual experts. For the second, reinforcement learning or other adaptive expert-selection strategies may help shorten the context without sacrificing decision quality. Another promising direction is to extend AgentFoX with MLLMs as high-level semantic experts, enabling reasoning about compositional inconsistencies and physical implausibilities beyond low-level artifact detection. Reducing inference overhead while preserving interpretability and reliability is therefore an important direction for future work.

Expert Profile For DRCT

Fundamental Description

Model: DRCT (Reconstruction Residual)

Analogy: The Re-enactment Lab

Core Mechanism: Uses contrastive learning across four image categories: Real, Fake, Real-Reconstructed, and Fake-Reconstructed. Reconstructing real images produces challenging "hard positive" samples, pushing the model to learn subtle, intrinsic fingerprints of a specific generative architecture.

Primary Use Case: Designed to capture intrinsic architectural fingerprints of generative models, particularly diffusion models, enabling strong generalization to unseen generators within the same class (e.g., transferring from one diffusion model to another).

Calibration Performance

Observation: DRCT was initially under-calibrated (ECE = 0.193), indicating a substantial gap between predicted probabilities and observed frequencies. After calibration, ECE fell to roughly 0.022, with probability estimates closely tracking outcomes. F1 also improved, showing that greater reliability coincided with better classification.

Interpretation: Calibration delivered a large gain for DRCT, reducing ECE from 0.193 to 0.022 and demonstrating high efficacy on models with weak initial calibration. The baseline F1 was 73.5%, and post-calibration it was maintained or improved, indicating that probability recalibration did not disrupt learned representations. Post-calibration ECE stabilized between 0.015 and 0.022, standardizing uncertainty estimates while preserving DRCT's performance profile.

Comparative analysis: DRCT exemplifies a "transformative enhancement" pattern—simultaneous improvements in calibration and F1 consistent with the correction of systematic prediction biases.

Reliability Assessment

Overall Evaluation: Exceptional success. The model moved from conservative and poorly calibrated to well-balanced and reliable.

Calibration: Probability estimates now closely match actual outcomes, with much lower calibration error. Confidence scores are trustworthy.

Performance: Reliability and accuracy improved at the same time. The conservative bias was corrected, producing more balanced predictions while keeping high precision.

Practical impact: (1) Detects more authentic/manipulated cases without losing accuracy; (2) Confidence scores support decision-making and risk assessment.

Deployment recommendation: Strongly recommended. Suitable for immediate deployment in high-stakes image authenticity detection, for both automated systems and human-in-the-loop workflows.

Strategic value: Calibration removed systematic biases, resulting in a more robust and trustworthy model for real-world use.

Figure 8. **Representative Expert Profile (DRCT).** Example of the textual description, calibration summary, and reliability information provided to the LLM agent for the DRCT detector.

Clustering Description

Applies Spatial Rich Model (SRM) filters to extract residual images through convolution operations, then computes Gray Level Co-occurrence Matrix (GLCM) on the residuals to derive texture statistics including contrast, correlation, energy, and homogeneity. These features capture

Clustering Analysis

The SRM-based clustering exhibits the strongest performance among all methods with a Silhouette Score of 0.230 and the best overall quality score of 0.808. The Davies-Bouldin score of 1.22 indicates relatively good cluster separation, making this the most effective approach for texture-based authenticity detection. The method successfully identified 9 distinct clusters with notable size variation (std: 210.9), including two large clusters (840 and 721 samples) that likely represent dominant texture patterns in authentic or generated images. The exceptionally high Calinski-Harabasz score of 1358.71 demonstrates strong between-cluster variance, confirming that SRM features effectively capture distinguishing texture characteristics. Despite being classified as 'weakly_clusterable' (confidence: 0.49), the Hopkins statistic of 0.844 actually suggests some clustering tendency exists, though the near-zero variance CV (4.14e-15) indicates potential feature scaling issues that should be addressed. The high feature correlation (0.467) suggests redundancy that could be reduced through feature selection. For practical deployment, this clustering is highly valuable for forensic analysis and tampering detection, as the texture statistics from GLCM effectively capture manipulation artifacts. The larger clusters likely represent common texture patterns in either authentic images or specific generation techniques, while smaller clusters (184-200 samples) may identify unique manipulation signatures. Recommendations include applying feature selection to reduce correlation

Clustering Profile For SRM

Clustering Performance

cluster_0: "DRCT excels in this cluster through its reconstruction-based contrastive learning, effectively capturing architectural fingerprints that manifest in the SRM-detected texture patterns. The reconstruction process amplifies subtle generative artifacts correlating with these textures. SPAI shows moderate performance, leveraging spectral analysis to identify frequency inconsistencies related to texture variations, though not as effectively as DRCT's spatial approach. RINE underperforms, suggesting the CLIP intermediate representations don't optimally encode the low-level texture characteristics emphasized by SRM filtering. Patch_Shuffle performs poorly as its context-disruption approach conflicts with the coherent texture patterns that require preserved spatial relationships for detection.",

cluster_1: "RINE dominates with exceptional performance, indicating strong alignment between SRM texture patterns and specific CLIP intermediate representations. The multi-layer fusion and Trainable Importance Estimator effectively emphasize layers encoding these patterns. SPAI and DRCT show moderate performance, suggesting both spectral and reconstruction approaches partially capture the textures but miss the specific features RINE detects. Patch_Shuffle exhibits particularly poor performance, confirming that the texture patterns require intact spatial relationships that shuffling destroys.",

cluster_2:

Figure 9. **Representative Clustering Profile (SRM).** Example of an SRM-based profile listing cluster-level reliability rankings of all expert detectors, used for context-aware arbitration.

Guidelines

Role Definition
 You are an expert AIGC Image Forensics Analyst. Reasoning Framework: ReAct paradigm (Observe → Reason → Act → Reflect).

Core Mission: Integrate evidence across semantic, pixel-level, and feature-cluster dimensions; quantify cross-dimensional conflicts and assess the confidence level of each finding.

Analysis Workflows

- 1. semantic_level**
 - **Objective:** Identify physical impossibilities and logical inconsistencies in scene content.
 - Evaluate, from the semantic perspective, whether the image is AI-generated.
- 2. expert_results**
 - **Objective:** Apply multiple forensic expert models or tools for technical analysis.
 - Document each model's findings and evaluate the confidence score for each model.
 - Record any conflicts among model outputs.
 - Note: Forensic model outputs may exhibit domain-specific biases; comprehensive cross-model evaluation is essential for reliable conclusions.
- 3. expert_analysis**
 - **Objective:** Synthesize and interpret expert model findings.
 - Retrieve expert profiles to determine how many expert models are available within the tool.
 - Use the model names to obtain the corresponding forensic results for each expert.
 - Summarize and interpret the forensic results.
 - Note: Subject qualitative and subjective interpretations to rigorous scrutiny for consistency and evidentiary support.
- 4. clustering_analysis**
 - **Objective:** Evaluate multi-expert outputs through clustering analysis.
 - Perform clustering across multiple feature dimensions to characterize each model's performance and relative strengths.
 - Integrate clustering findings with prior analyses to establish confidence levels and reliability metrics for each analytical model.
 - Do not use clustering results as the basis for final decision-making because per-image cluster quality is poor.
 - In clustering, metrics such as F1-score and Precision reflect performance on specific clusters within the validation set. While useful for comparing models, their reference value is limited due to domain shift and should be interpreted with caution.
- 5. conflicting_resolution**
 - **Objective:** Agentic Autonomous Analysis.
 - Consider the semantic context and expert model predictions jointly. Aggregate experts with appropriate weights to produce a unified decision and confidence.
 - Provide a transparent record of conflict sources, chosen context (or out-of-distribution), key weights, any fallbacks, and the rationale; use clustering only for weighting and calibration, not as the final decision rule.
- 6. finally_report**
 - **Objective:** Produce a comprehensive inference on whether the image is real or AI-generated based on all information.
 - Result summary: Summarize the semantic assessment and the forensic outputs of each expert model.
 - Confidence estimation: Estimate confidence levels for each dimension (semantic, pixel-level, subjective analysis).
 - Justification: Provide detailed reasoning documenting how disagreements are resolved and explain how confidence scores are weighted and reconciled to reach the final decision.
 - Final Decision: 0 (natural image) / 1 (AI-generated image)
 - End Identify: "Update stage to: done" Note: If your conclusion differs from those of all experts, you should provide sufficient evidence to support your judgment

Analysis Principles

- Before invoking any tool, perform ReAct and present the process in your reply.
- After obtaining tool results each time, analyze and reflect on them, then select the next tool to invoke or terminate the pipeline. Add "Update stage to: [next stage name]" at the end.
- If a tool call fails, analyze the cause and retry once, but do not invent tool outputs; if tools remain unavailable or continue to fail, immediately disclose the exception and return "Update stage to: error".
- At the end of each of your responses, add: "Update stage to: [stage_name]"

{Tool names} **Conversation History**
{Tools} **{messages}**

Figure 10. **Forensic Guideline.** The rule-based system prompt that governs AgentFoX's structured multi-stage reasoning workflow and serves as the protocol followed in the detailed trace shown in Figure 11.

Image Authenticity Analysis

Semantic Analysis Summary

- No substantive anomalies in optical physics, geometric consistency, or texture coherence.
- Laplacian value of 279.1725 indicates sufficient edge detail.
- Frequency-domain energy distribution appears natural.
- No AI-typical artifacts (e.g., deformed features, unnatural symmetry) detected.

Limitations:

- Low resolution (256×256) may mask fine-grained artifacts.
- Moderate compression ratio (1.915) can slightly affect texture and boundary cues.
- Lack of occlusions and scene ambiguity simplifies interpretation but reduces opportunities to expose hidden artifacts.

Expert Model Analysis

- DRCT: prediction 0.9735; calibrated 0.9261 → **AI-generated: Yes**
- SPAI: prediction 0.0011; calibrated 0.1872 → AI-generated: No
- RINE: prediction 0.9874; calibrated 0.9614 → **AI-generated: Yes**
- PatchShuffle: prediction 0.4469; calibrated 0.6327 → **AI-generated: Yes**

Model Performance Context:

- DRCT: High confidence (92.61% calibrated). Designed to capture diffusion-model artifacts; strong cross-generator generalization.
- RINE: Very high confidence (96.14% calibrated). Robust to compression and cropping; strong cross-generator detection.
- SPAI: Low confidence (18.72% calibrated), likely constrained by spectral analysis on low-resolution inputs.
- PatchShuffle: Moderate confidence (63.27% calibrated). Effective for local texture cues but less decisive in ambiguous cases.

Clustering Analysis Insights

- SRM clustering (best performance):
 - Silhouette score: 0.224 (moderate separation).
 - Davies–Bouldin score: 1.19 (indicative of strong cluster separation).
 - RINE dominance: 46.7% F1 and 46.7% precision in cluster 5, consistent with robust texture-based detection.
- CFA clustering (moderate performance):
 - PatchShuffle strength: 61.68% F1 in cluster 7, highlighting effectiveness on local texture patterns.
 - DRCT weakness: 42.8% F1, suggesting limited sensitivity to CFA-specific artifacts.

Implications:

- SRM clustering is the most reliable among tested settings for texture-driven forensics.
- CFA clustering favors local-texture methods (PatchShuffle) over global methods (DRCT).

Conflict Resolution and Confidence Estimation

- DRCT/RINE vs. SPAI:
 - DRCT and RINE strongly indicate AI generation, while SPAI suggests authenticity. This divergence stems from methodological focus:
 - DRCT/RINE emphasize architectural fingerprints and intermediate representations.
 - SPAI leverages spectral-domain cues, which are less reliable at 256×256.
 - PatchShuffle aligns with DRCT/RINE but with only moderate decisiveness.
- Confidence weighting:
 - Semantic analysis: Low (2/5) given resolution/compression constraints.
 - DRCT/RINE: High (4.5/5) based on calibrated scores and known strengths.
 - PatchShuffle: Medium (3.5/5) due to moderate reliability in ambiguous cases.
 - SPAI: Low (2/5) owing to poor calibration under low-resolution conditions.
- Justification:
 - DRCT and RINE offer strong, calibrated evidence (92.61% and 96.14%).
 - PatchShuffle moderately supports the AI-generated hypothesis (63.27%).
 - SPAI's counter-indication is discounted due to spectral-domain limitations at this resolution.
 - Clustering results (SRM and CFA) are consistent with AI-generation signals; combined clustering is unreliable and not used for the final call.



Final Decision

Conclusion: **The image is likely AI-generated**

Confidence level: High (4.2/5).

Figure 11. **Detailed reasoning trace under the Forensic Guideline.** AgentFoX analyzes a challenging AI-generated image, identifies conflicting expert signals, consults the relevant Clustering Profile, down-weights experts that are unreliable in the matched cluster, and reaches an evidence-grounded final verdict with a transparent forensic report.